

Separated-oscillatory-field measurement of the $n = 10 \ ^+F_{3-} \ ^+G_4$ interval in helium: A 200-part-per-billion measurement

C. H. Storry, N. E. Rothery, and E. A. Hessels

Department of Physics, York University, 4700 Keele Street, Toronto, Ontario, Canada M3J 1P3

(Received 19 June 1996)

The $n = 10 \ ^+F_{3-} \ ^+G_4$ energy interval in helium is measured to an accuracy of 200 parts per billion. Rydberg states of helium are created by charge exchange between a helium ion beam of a few keV and a dense thermal beam of neutral cesium atoms. A microwave transition is driven between the two states in a Ramsey-separated-oscillatory-field configuration yielding a linewidth of less than 0.2 MHz. The result of 2017.3254(4) MHz is the most accurate measurement of any Rydberg fine structure and can be compared to a similarly accurate theoretical prediction of this interval. This comparison gives a very high-precision test of physics on the large-distance scale of these Rydberg states, including the nonrelativistic Coulomb potential, relativistic effects, and quantum-electrodynamical effects such as the retardation (or Casimir) interactions. A disagreement between theory and experiment indicates the possibility of additional new physics on this distance scale. [S1050-2947(97)06901-1]

PACS number(s): 32.30.Bv, 31.30.Jv

INTRODUCTION

The Rydberg states of helium have proven to be very useful for testing the physics of two-electron atoms, and in particular for testing long-range interactions in atomic systems. During the past 15 years, the accuracy with which these Rydberg intervals have been calculated has greatly improved. The accuracy of experimental measurements has also continued to improve, and thus the physics of this atom has been tested with increasing accuracy.

The $n = 10 \ ^+F_{3-} \ ^+G_4$ interval was measured by Farley, MacAdam, and Wing [1] in 1979 using a microwave-optical technique with helium gas excited by electron bombardment. (Here the notation $^{2S+1}L_J$, where L , S , and J are the orbital, spin, and total angular momenta, respectively, has been modified since S is not a good quantum number for this system. The label “+” indicates the higher energy of the two states which are mixtures of singlet and triplet $J=L$ states.) In a series of measurements [2], D - F and D - G intervals in $n = 6$ – 16 were measured, and the $10 \ ^+F_{3-} \ ^+G_4$ interval in particular was measured to an accuracy of about 300 kHz or 150 parts per million (ppm). Measurements of somewhat higher accuracy were done [3] in $n = 7$ and 8 F - G , F - H , and F - I intervals by Cok and Lundeen, who used a fast atomic helium beam produced by charge exchange between a 10-keV He^+ beam and a neutral gas. They measured the $n = 8 \ ^+F_{3-} \ ^+G_4$ interval to an accuracy of 106 kHz, or 30 parts per million. In 1984, Palfrey and Lundeen [4] introduced a detection technique in which $n = 10$ Rydberg atoms are excited up to a very-high- n state using a CO_2 laser, and subsequently ionized. The technique resulted in a significant improvement in the precision of these Rydberg measurements, yielding $n = 10$ G - H , H - I , and I - K measurements at a precision of 10 kHz (20–160 ppm). Subsequent refinements of the Palfrey technique have allowed a series of measurements [5–8] of the $n = 10$ D - F , F - G , G - H , H - I , and I - K intervals at a precision of nearly one part per mil-

lion. In particular, the $n = 10 \ ^+F_{3-} \ ^+G_4$ interval was measured [6] to an accuracy of 3.1 kHz, or 1.5 parts per million. Recently, all of the $n = 5$ F - G intervals were measured by Kriescher, Hilt, and Oppen [9], using ion impact to excite thermal helium. The precision of the $n = 5 \ ^+F_{3-}$ -to- $^+G_4$ interval was 80 kHz, or 5 parts per million. We report here a measurement of the $10 \ ^+F_{3-} \ ^+G_4$ interval in helium using microwaves in a Ramsey-separated-oscillatory-field geometry. The accuracy of the measurement is 200 parts per billion (almost an order of magnitude improvement over the previous measurement which did not employ separated oscillatory fields) and is the most precise measurement of any Rydberg fine-structure interval. A brief report of these results has been given earlier [10].

The theory of highly excited states of helium has also improved dramatically in recent years. For higher- L states, accurate nonrelativistic energy levels have been obtained by Drachman [11] using a polarization model. Various relativistic and quantum-electrodynamic corrections have also been calculated in the long-range polarization formalism [11,12,13]. For the 10 F and G states, accurate energies became available in 1989, when Drake extended his very precise S , P , and D [14] variational calculations up to the F and G states [15]. In these variational calculations [16,17], the nonrelativistic energies are obtained to essentially exact precision using a clever choice of variational wave functions, and the relativistic and quantum-electrodynamic corrections are calculated using these wave functions. The two very different methods of calculation (polarization-model calculations at high L and variational calculations at lower L) have been applied to the I and K states and both give very accurate energy predictions for these states. Thus many aspects of both methods of calculation can be tested by comparison of contributions to these states [18]. The most precise calculation of the $10 \ ^+F_{3-}$ -to- $^+G_4$ energy interval is from Drake's calculations [16]. The uncertainty in the predicted interval is 400 Hz or 200 parts per billion. Combined with the present 200-part-per-billion measurement, it forms a precision test of the physics in the helium Rydberg atom.

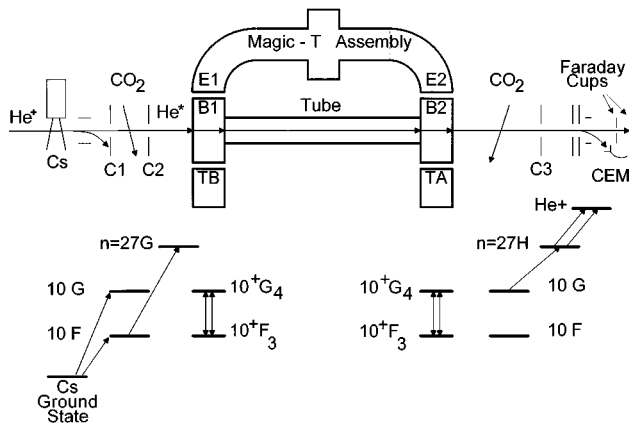


FIG. 1. Schematic diagram of the experiment along with an energy-level diagram. The helium ion beam is neutralized in a dense thermal cesium beam. Unneutralized ions are deflected downward in field of 8 kV/cm. A CO₂ laser beam creates a population difference between the 10*F* and 10*G* states by emptying the 10*F* state into the 27*G* state. The microwaves in the SOF configuration stimulate the 10⁺*F*₃-to-⁺*G*₄ transition at 2 GHz. A second CO₂ laser beam excites the remaining 10*G* atoms up to the 27*H* state and these *n*=27 atoms are Stark ionized in an electric field of 3.7 kV/cm. The resulting ions are deflected into a CEM detector. The remaining neutral beam continues onto a three-section Faraday cup which monitors the beam direction and intensity.

EXPERIMENT

In the present experiment, microwaves in a separated-oscillatory-field (SOF) geometry are used to drive the *n*=10⁺*F*₃-to-⁺*G*₄ transition in a fast atomic beam of helium atoms. The present work is an application of the separated-oscillatory-field technique to the precision study of the fine structure in Rydberg states. The advantages of using a SOF geometry are reduced linewidth, more extensive experimental tests of systematic effects, and near elimination of one of the major systematic effects in previous fast atomic beam measurements, namely, the first-order Doppler shift. These advantages have been employed in many atomic measurements [19] since the method was proposed by Ramsey [20].

A schematic of the experimental setup is shown in Fig. 1. Helium ions are created using a Colutron model G-2-D ion source (not shown in Fig. 1) with a spread in beam energy of less than 1 eV. Half of the data are taken with 4.001(1)-keV ions, while the other half are taken with ions at 2.309(1) keV. These potentials are measured at the anode of the ion source to an accuracy of 0.02% using a precision voltage divider (Julie Research Labs model KV VB-10) and a HP multimeter (model 34401A).

The ions are neutralized in a dense thermal beam of cesium atoms. The cesium beam is produced by heating a stainless steel container of cesium metal to a temperature of 440 K. The cesium beam has a density of 10¹⁴ atoms/cm³ just outside of a 2.5-mm-diam hole in the 2.5-mm-thick wall of the container. The hole is situated such that the cesium beam is downward pointing (so as to avoid clogging of the hole) with the ion beam passing within a couple of millimeters of the opening. The cesium is collected on a cooled brass cup maintained at -50 °C and situated approximately 5 cm below the cesium source. More than half of the ions are

neutralized in the cesium beam, with a small fraction of them being neutralized into *n*=10 states. This method is much more efficient at producing *n*=10 states than charge exchange with neutral gases such as argon, CH₄, or helium, presumably because of the small binding energy of the cesium outer electron. Another method of charge exchange which was demonstrated in a recent measurement [21] employs a neutral cesium target which is itself excited up to a Rydberg state using a two-step laser excitation. Although this method of resonant charge exchange is found to produce a very large number of *n*=10 helium atoms, the fraction of ions neutralizing into *n*=10 decreases as the number density of the cesium increases. The decrease is presumably due to collisional processes in the cesium, as well as more exotic radiative processes [22]. Due to this decrease, and because the laser-excited target is less stable, the high-density ground-state cesium target is employed for the present measurement.

Helium ions not neutralized in the cesium target are deflected out of the beam by an electric field of 8 kV/cm. This field also ionizes very-high-*n* atoms which would otherwise ionize in our detection region and contribute to the background signal.

The neutral helium beam is collimated at C1, C2, and C3 in Fig. 1, which confine the vertical size of the beam to 1.0, 1.1, and 3.0 mm, respectively. To accurately position these collimators, as well as other components along the beamline, a high-power surveyor's scope is employed. It is mounted on a heavy steel support which is bolted securely to the laboratory floor about 4 m beyond C3, and is not moved during the experiment. With this scope it is possible to determine the position of components along the beamline to accuracies of better than 15 μm. It was directly verified that the axis defined by the scope (i.e., the position observed at the crosshairs of the scope as it is focused to distances of 4.0–5.5 m) forms a straight line to this accuracy. The collimators are centered on the axis defined by the surveyor's scope to a precision of 0.13 mm for C1 and C2 and 0.25 mm for C3. The distances between the collimators are 28 cm (between C1 and C2) and 122 cm (between C2 and C3). The collimators put limits on the possible variation in the direction of the helium atoms and then are not moved during the entire set of measurements.

Both 10*F* and 10*G* atoms are produced in the target. A population difference between the *F* and *G* states is created by selectively exciting 10*F* atoms up to the 27*G* state (between C1 and C2 of Fig. 1). For this purpose a ¹²C¹⁸O₂ laser supplied by Ultra Lasertech (model PX3500GL) is tuned to the *IP*(26) line (λ=10.563 μm) yielding about 4 W of output power, half of which is used here. This laser excites approximately one-half of the 10*F* atoms up into the 27*G* state. Fine tuning of the laser frequency is accomplished by changing the angle of intersection of the laser beam with respect to the atomic beam axis, thus varying the Doppler shift of the laser frequency in the frame of the atoms.

The beam is collimated at C2 and enters the separated-oscillatory-field region, in which the *n*=10⁺*G*₄-to-⁺*F*₃ microwave transition is stimulated. This region consists of microwave regions B1 and B2 (see Fig. 1) with a 5-cm-inner-diam tube connecting them. B1 and B2 are precision machined waveguide sections which are identical in all di-

mensions to within less than $25 \mu\text{m}$. Each is constructed out of two solid copper blocks machined into channel-shaped troughs. Dowel pins are used to precisely align the troughs with each other as they are bolted together. The inner dimensions of the resulting waveguide ($5.461 \times 10.922 \text{ cm}$) match those of the WR430 waveguide to better than $25 \mu\text{m}$. The beam passes through $B1$ and $B2$ via $1.016 \times 2.032 \text{ cm}$ holes centered on both sides of the 10.922-cm dimension of the waveguide sections.

The microwaves are generated by an Anritsu model MG3602A signal generator, the time base of which is stabilized to an accuracy of 10^{-11} using a highly stable 10-MHz reference signal from a Stellar model 100B satellite connection to the Global Positioning System (GPS) time base. A Narda (model SS122DHS) single pole double throw switch driven at 221 Hz alternately directs the microwaves to the E and H input ports of a Struthers (model M352M) waveguide Magic T. The connections are made via type- N cables which pass into the 1-m-diam vacuum chamber using Amphenol UG-300/U vacuum feedthroughs. Inside the vacuum chamber, type- N cables are used for the connection to Scientific Atlantic (model 11-1.7) type- N -coax-to-WR430-waveguide adapters. When microwaves are input to the H input port of the Magic T, the microwaves leaving the two output ports of the Magic T are very nearly in phase; when the input is to the E input port, the microwaves leaving the two output ports are very nearly 180° out of phase. The two output ports of the Magic T are each connected to a 14.60-cm section of WR430 waveguide followed by a Struthers (model E130M) right-angle waveguide E bend. This combination of two type- N -coax-to-WR430-waveguide adapters, Magic T, two 14.60-cm waveguide sections, and two E bends is referred to as the Magic-T assembly. The whole assembly is constructed such that the output flanges of the two bends $E1$ and $E2$ (see Fig. 1) are square and coplanar with each other and such that the flanges are separated by $98.095(25) \text{ cm}$ (center to center). The waveguide sections $B1$ and $B2$ are secured solidly in the vacuum chamber such that they are accurately positioned in the same pattern: square to each other, coplanar, and with the same 98.095-cm separation (to within 0.0025 cm). The centers of $B1$ and $B2$ are viewed through the surveyor's scope and each is within $25 \mu\text{m}$ of the axis defined by the scope. Because they are square to each other, coplanar, and aligned along the scope's axis, $B1$ and $B2$ are perpendicular to this axis to within 0.03 mrad .

$B1$ and $B2$ are left in position for the entire duration of the experiment. Due to the precise positioning of $B1$ and $B2$ and the precise construction of the Magic-T assembly, it is possible to make precisely matched connections between $E1$ and $E2$ of the Magic-T assembly and either the top or the bottom of $B1$ and $B2$, and also to attach either end of the assembly ($E1$ or $E2$) to either $B1$ or $B2$. Thus the Magic-T assembly can be oriented in four different ways. Dowel holes in $B1$, $B2$, $E1$, and $E2$ and the dowel pins used in the connections are machined with a tolerance of better than $25 \mu\text{m}$, ensuring precisely matched connections in all four possible configurations.

Three sets of data are taken in each of the four different orientations of the Magic-T assembly, and hence the orientation of the Magic-T assembly is changed 12 times during the course of the measurement. Each time the Magic-T as-

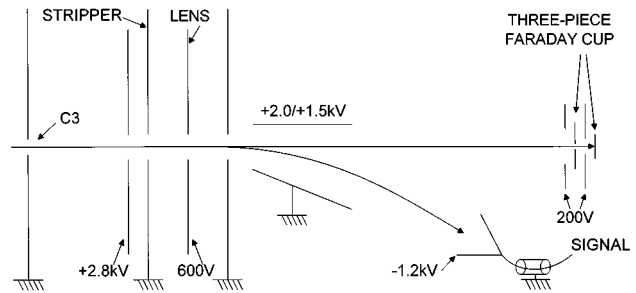


FIG. 2. Detection region. A field of 500 V/cm between the first pair of copper plates ionizes very-high- n states which would otherwise contribute to the background signal. $n=27$ states created in the laser-interaction regions are stripped between the next pair of plates in a field of 3.7 kV/cm . The lens focuses the resulting ion beam, which is then deflected downward into a CEM detector. The remaining neutral beam continues onto a three-section Faraday cup used to monitor beam direction and intensity.

sembly is reoriented, the positions of $B1$ and $B2$ are checked relative to the axis of the high-power surveyor's scope, and they do not move by more than $50 \mu\text{m}$. In addition, the fact that the dowel holes in $B1$ and $B2$ continued to align with the dowel holes in $E1$ and $E2$ of the Magic-T assembly indicates that the relative position of $B1$ and $B2$, as well as the structure of the Magic-T assembly, is unaltered (to a precision of $25 \mu\text{m}$) throughout the measurement.

The microwaves are absorbed after the waveguide sections in a pair of Struthers model 200M precision waveguide terminators, TA and TB, which have very small microwave reflections ($|\Gamma| \sim 0.025$) that are measured using a slotted line (Microlab-FXR model R101B). TA is attached to $B2$ and TB is attached to $B1$ using dowel pins.

After the microwave regions, the atomic beam enters a second laser-interaction region, where the other half of the CO_2 laser beam is used. The laser frequency is again Doppler tuned, this time to excite the $10G$ -to- $27H$ transition. The purpose of this laser interaction is to determine how many of the $10G$ atoms have been driven into the $10F$ state by the microwaves. This 2-W laser beam is chopped with an optical chopper (Stanford Research Systems model SR540) at 470 Hz (with a 90%-on, 10%-off duty cycle) and excites approximately one-half of the $10G$ atoms up to the $27H$ state.

Four centimeters past the second laser-interaction region the atomic beam enters the detection region through collimator C3. The first half of the detection region (see Fig. 2) consists of a series of five 0.9-mm -thick copper plates with narrow slots cut in them. The slot in the first (C3) is 3.0 mm in height and the next four are 3.4 mm in height. C3, at ground, is separated by 5.4 cm from the stripper plate which is maintained at $+2.8 \text{ kV}$. Between these plates very-high- n states are Stark ionized, reducing the background signal to which they would otherwise contribute. The next plate is grounded and separated by 0.76 cm from the high-voltage plate. As the $n=27$ states created in the laser-interaction regions enter the field of 3.7 kV/cm between these two plates, they are Stark ionized, and the resulting ions are accelerated by approximately 2.8 kV in the field. The next pair of plates form a lens used to focus these ions. The lens is found to give only a small increase in signal size and is set at 600 V . The ions are deflected downward into a channel elec-

tron multiplier (CEM) (Galileo model 4720) by a pair of plates 5 cm long which are separated by 1.4 cm at one end and 3.7 cm at the other (see Fig. 2). The bottom deflection plate is maintained at ground and the top is set to +2 and +1.5 kV for the 4.0- and 2.3-keV atomic beams, respectively. The CEM has a -1.2-kV potential applied to its front face. The result is a 10-nA current (primarily a dc background) which is directed into a Melles Griot large dynamic range current amplifier.

The output signal from the current amplifier is fed into two lock-in amplifiers. The microwave signal, the signal synchronous with the switching of the microwaves between the two input ports of the Magic T, is extracted with an EG&G (model 5105) lock-in amplifier referenced to the 221-Hz switching rate of the microwave switch. A second signal is extracted by a lock-in amplifier (Stanford Research Systems model SR850) referenced to the 470-Hz chopping frequency of the CO₂ laser beam. This signal is used as a diagnostic and to normalize the main microwave signal.

The remaining neutral beam continues onto a three-section Faraday cup, each section of which is a 0.9-mm-thick piece of copper. The top and bottom sections are separated vertically by 1.5 mm and the pair is centered on the axis of the surveyor's scope to within 0.4 mm. The third section is positioned 1.9 cm behind the top and bottom sections and thus monitors the central 1.5 mm of the beam. The top and bottom sections remain in place for all of the measurements, whereas the central section is removable to allow the collimators, waveguide blocks, and the top and bottom sections of the Faraday cup to be viewed with the surveyor's scope. Neutral atoms hitting these Faraday cups cause electrons to be ejected and these electrons are collected on nearby copper plates biased at +200 V. The combined current on the Faraday cups is approximately 5 μ A, indicating a total of approximately 3×10^{13} neutral atoms per second are in the collimated beam. The relative signal on each of the three Faraday cups gives a measure of the beam's direction. By adjusting the focusing parameters of the ion source it is possible to maintain constant relative currents on the three Faraday cups to within 10%. The constant ratio indicates that the vertical position (at the Faraday cups) of the center of the neutral beam does not vary by more than 0.05 mm. The direction of the atomic beam is determined by this well-defined position of the beam at the Faraday cups and by where the center of the beam is positioned as it passes through the 1.0-mm first collimator (C1). It is estimated that the center of the beam is within 0.25 mm of the center of this 1.0-mm collimator, with possible variations of position within this ± 0.25 -mm range as the ion focusing and deflecting optics of the ion source are varied from day to day. Since the center of C1 is within 0.13 mm of the surveyor's scope axis, the Faraday cups (which are 1.5 m down the beamline) are within 0.4 mm of this axis, and B1 and B2 are perpendicular to the scope axis to within 0.03 mrad, we conclude that the direction of the center of the beam is perpendicular to the direction of the microwave propagation to within 0.3 mrad, with possible variations in this direction from run to run of 0.2 mrad.

The data are taken in 12 runs of data acquisition, with each set taken on a separate 20-h day. Each data run includes data taken at acceleration voltages of 2.309(1) and 4.001(1)

kV. Most data are taken at a microwave power such that the transition is saturated and the rest of the data are taken at 6 dB lower power (i.e., approximately one-quarter of the saturation power). Additional data are taken each day to monitor small stray electric fields in the microwave region as described in the next section. Between data runs the orientation of the Magic-T assembly is changed and the vacuum chamber reevacuated to a pressure of about 6×10^{-7} torr.

LINE SHAPE AND FITTING

In the separated-oscillatory-field microwave system the atoms pass through the two regions of microwave field (in B1 and B2). These regions are 5.4610(25) cm across, corresponding to a time in each field of $\tau_{4.0 \text{ kV}} = 0.1243 \mu\text{s}$ and $\tau_{2.3 \text{ kV}} = 0.1637 \mu\text{s}$ for atoms at the two beam speeds ($\beta_{4.0 \text{ kV}} = 0.001465$ and $\beta_{2.3 \text{ kV}} = 0.001113$ for the 4.001- and 2.309-keV beams). The distance from the center of B1 to the center of B2 is 98.095(25) cm, corresponding to transit times of $T_{4.0 \text{ kV}} = 2.233 \mu\text{s}$ and $T_{2.3 \text{ kV}} = 2.939 \mu\text{s}$. These are considerably larger than the 1.08- and 1.81- μs radiative lifetimes of the 10F and 10G states. (The radiative lifetimes of the other two states used in the experiment, the 27G and 27H states, are 36 and 54 μs , respectively.)

The Hamiltonian that drives the microwave transition is

$$H(t) = eEz g(t), \quad (1)$$

where

$$g(t) = \cos(2\pi ft) \times \begin{cases} +1 & \text{for } -\left(\frac{T}{2} + \frac{\tau}{2}\right) \leq t \leq -\left(\frac{T}{2} - \frac{\tau}{2}\right) \\ 0 & \text{for } -\left(\frac{T}{2} - \frac{\tau}{2}\right) \leq t \leq \left(\frac{T}{2} - \frac{\tau}{2}\right) \\ \pm 1 & \text{for } +\left(\frac{T}{2} - \frac{\tau}{2}\right) \leq t \leq +\left(\frac{T}{2} + \frac{\tau}{2}\right). \end{cases} \quad (2)$$

The ± 1 indicates the microwaves in the second region are 0° or 180° out of phase of those in the first region. Here f is the frequency of the applied microwaves, E is the amplitude of the microwave electric field, and eEz gives the electric dipole along the z direction. The field shape $g(t)$ includes an assumption that the microwave fields turn on and off suddenly as the atoms enter and exit the microwave regions. Using time-dependent perturbation theory (to lowest order) one obtains the line shape for this transition:

$$\sum_{m_J = -3}^3 \left[\frac{2eEz_{fg}^{m_J}}{\Delta E_{fg} - hf} \sin[\pi\tau(f_{fg} - f)] \right]^2 \cos[2\pi T(f_{fg} - f)]. \quad (3)$$

This line shape is the difference between the probability of driving the 10^+F_3 -to- $^+G_4$ transition when the two regions are in phase [+1 case in Eq. (2)] and the probability when they are 180° out of phase [-1 case in Eq. (2)]. Here, ΔE_{fg} (which equals hf_{fg}) is the energy difference between the F and G states and $z_{fg}^{m_J}$ is the z matrix element evaluated be-

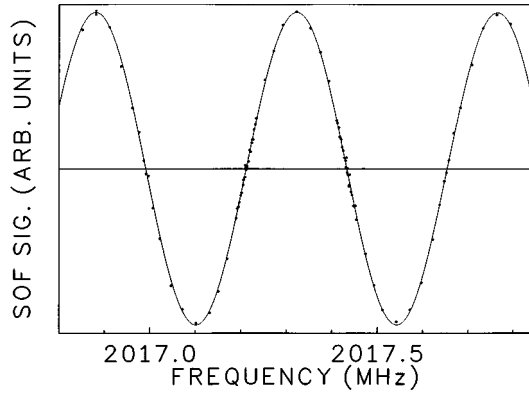


FIG. 3. Data taken at 4.001 keV. The experimental data are shown as solid points and a typical sized error bar is given on the point at 2016.83 MHz. The solid line is a least-squares fit to a simple cosine function. Note the excellent agreement between this expected shape and the data.

tween these two states. Since the value of $z_{fg}^{m_j}$ varies with m_j (the J_z quantum number), a sum is taken over all participating m_j states. The factor in square brackets is the Rabi envelope which is centered at $f=f_{fg}$ and has a width of $1/\tau$ or 8.045 and 6.109 MHz for the 4.001- and 2.309-kV beams. The cosine factor gives the Ramsey-SOF oscillations and these are also centered at $f=f_{fg}$. For the small τ 's of the present measurement, the Rabi envelope changes very little for frequencies near f_{fg} , and hence the SOF oscillations are approximated well by the cosine function: $A \cos[\Omega(f-f_{fg})]$. The data for the measurement are taken within a range 0.5 MHz on either side of the resonance. The data taken at the fast beam speed are shown in Fig. 3 and fit very well to a cosine function (solid line).

An analytic form giving a more correct line shape for the transition amplitude in a separated-oscillatory-field microwave system is obtained by Lundeen and Pipkin [23]. This form does not use a weak-field approximation (as the perturbation theory does) and includes the lifetimes of the two states. It still assumes a two-level system and that the microwave fields turn on and off suddenly as the atoms enter and exit the microwave regions. This line shape still indicates Ramsey-SOF oscillations centered about $f=f_{fg}$, and for frequencies near $f=f_{fg}$ is still well approximated by a cosine function.

The expected line shape is further investigated using a full numerical integration of the Schrödinger equation. The integration includes all of the $10D$, $10F$, $10G$, and $10H$ states. Energies for the states are from Drake [16] and hydrogenic lifetimes for the states are also included. All four states of each L , and all m_j states are included in the modeling. The z matrix element between each pair of states is calculated in the hydrogenic approximation. Further, the microwave fields are not assumed to turn on and off sharply. Since the 20-cm microwave wavelength is much larger than the hole size through which the atomic beam passes, the microwave fields are mostly confined to the inside of the waveguides. The fields do, however, extend a short distance beyond the holes in the waveguides, and hence the fields modeled here include an exponential ramping (up and down) of the microwave electric field amplitude. This ramping is such that the micro-

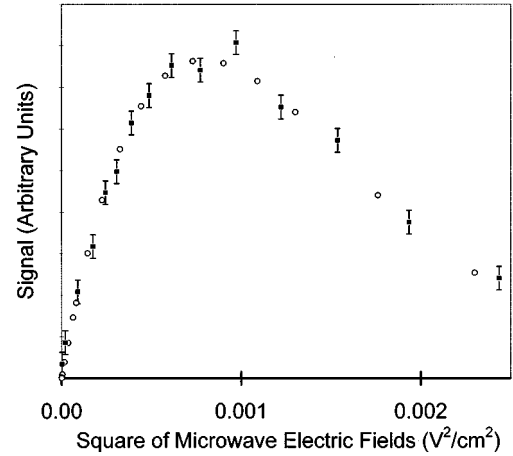


FIG. 4. Experimental and modeled saturation behavior of the resonance. The open points are the predicted signal on resonance obtained from numerical integrations. The points with error bars are experimental data. The experimental data are scaled to give the best agreement with the predicted saturation curve.

wave electric field amplitude is half its maximum value at the edge of the waveguide, drops to one-quarter at a distance of 0.5 cm (half the hole size) outside of the waveguide, and increases to three-quarters at 0.5 cm inside of the waveguide.

In the modeling, the complex wave function Ψ is obtained by numerically integrating the Schrödinger equation starting from 10 cm before $B1$ to 10 cm past $B2$. The integration uses approximately 3×10^6 steps; each step corresponds to the atom moving a distance of $0.5 \mu\text{m}$ along the atomic beam, or alternately a time step of about 1 ps (1 part in 500 of a single microwave oscillation). A fourth-order Runge-Kutta integration technique is used and the population after the microwave regions in the states is determined for the 0° and 180° relative phases of the SOF microwaves.

Integrations are done at a microwave frequency equal to the theoretical unshifted $n=10 \ ^+F_3$ -to- $\ ^+G_4$ energy difference using electric fields of 0 to 0.05 V/cm. The resulting predicted signal is plotted (open points) versus the square of the electric field in Fig. 4. Experimentally, a saturation curve is taken (points with error bars in Fig. 4) for input powers to the microwave system of -50 to -2 dB m. The axes of the experimental data are scaled to give the closest match to the predicted saturation curve. This scaling gives the most precise determination of the electric field present in the waveguides at a given input power. From the scaling, it is determined that the microwave electric field in $B1$ and $B2$ is 0.031 13(13) and 0.015 62(7) V/cm for the 4.001-kV data taken at approximately saturation power and at one-quarter saturation power. For the 2.309-kV data, the electric field is 0.023 62(10) V/cm at saturation and 0.011 84(5) V/cm at one-quarter saturation power.

Integrations were also done in each of these four cases (4.001- and 2.309-kV beams, at saturation and one-quarter saturation power) at microwave frequencies ranging from 2016.500 to 2017.925 MHz in 0.075-MHz steps. Figure 5 is an example of the results of such integrations. Again, because the frequency range is confined to near the center of the Rabi envelope, the results of the integration (solid dots) fit well to a cosine function (solid line in Fig. 5) which is of the form

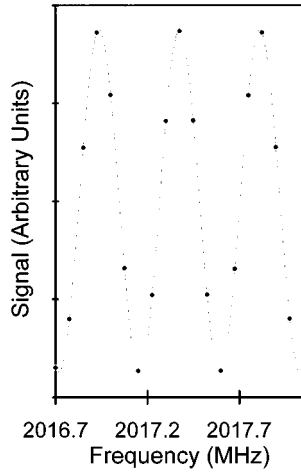


FIG. 5. Results from a typical numerical integration. The points are results of numerical integrations at 20 microwave frequencies near the resonance. The integration assumes equal population for all m_J states and are at $E=0.031$ 13 V/cm and an accelerating voltage of 4.001 kV. The solid line is a least-squares fit to the points using a cosine function.

$$A \cos[\Omega(f-f_0)] + C, \quad (4)$$

with the parameters A , Ω , f_0 , and C determined by a least-squares fit.

The parameter Ω is the oscillation frequency of the SOF signal. Time-dependent perturbation theory [Eq. (3)] predicts that this oscillation frequency Ω is $2\pi T$, or $\Omega_{4.0 \text{ kV}}=14.03 \mu\text{s}$ and $\Omega_{2.3 \text{ kV}}=18.47 \mu\text{s}$ for the fast and slow beams, respectively. For stronger fields, Ω shows a dependence on the dipole matrix element $eEz_{fg}^{m_J}$. This dependence is evident from the fits of the results of the numerical integrations for the different m_J states (which have different z matrix elements) and for different values of E . For the fast beam, the value of Ω obtained from the numerical integrations ranges from 14.17 to 14.53 μs for the different m_J states at saturation power and 14.07 to 14.09 μs at one-quarter power. When all seven m_J states are included (assuming equal initial population in each) the oscillation frequency Ω for the fast, saturation-power case is found to be 14.35(1) μs . The uncertainty here is due to the accuracy with which a cosine function [Eq. (4)] fits the results of the numerical integration. The Ω 's obtained from such fits are tabulated in Table I for the two beam speeds at the two powers at which data are taken.

TABLE I. The SOF oscillation frequency Ω . The modeled value in the third column is that expected from time-dependent perturbation theory. At higher powers the modeled value is the result of a fit of the numerically integrated results to the cosine function of Eq. (4). The experimental values are from fits of the experimental data to the same cosine function. One standard deviation uncertainties are given in parentheses. Note the good agreement between the modeled and experimental values.

		Perturbation theory	1/4 saturation power	Saturation power
Fast beam speed	Modeled	14.03 μs	14.08(1) μs	14.35(1) μs
	Experiment		14.10(4) μs	14.30(4) μs
Slow beam speed	Modeled	18.47 μs	18.55(1) μs	18.91(1) μs
	Experiment		18.55(14) μs	18.92(13) μs

Also listed in Table I are the oscillation frequencies Ω predicted from time-dependent perturbation theory and those found from the fits of the experimental data. The agreement between the experimental and theoretical Ω 's is a strong confirmation (at the level of a few parts per thousand) of the travel time T between the two microwave regions and hence the speed of the atoms. The agreement also confirms the microwave field amplitudes and the assumption that all m_J levels are equally populated.

The excellent agreement between (a) the results of the numerical integration and the expected cosine line shape (Fig. 5), (b) the results of the numerical integration and the experimental saturation curve of Fig. 4, and (c) the experimental and modeled oscillation rates Ω of Table I indicates that the experimental data are understood and accurately modeled by the numerical integrations of the Schrödinger equation.

The data of the measurement are the scans of microwave signal versus microwave frequency near the transition resonance. Three data sets were taken, each consisted of data with the Magic-T assembly in all four possible configurations and at the two beam speeds. Some data were taken with the transition saturated and some at one-quarter saturation power. These data and the scans of the $n=20$ $D-F$ resonance taken in the experiment are fit to the cosine function of Eq. (4). The centers from these fits are listed in the columns labeled ‘‘Fit center’’ in Tables II and III. Corrections due to various systematic effects (discussed in the next section) are applied to these fit centers and the corrected centers give the measurement of the $n=10$ $^+F_3$ -to- $^+G_4$ interval as shown in the final columns of Tables II and III.

SYSTEMATIC EFFECTS

As in all high-precision experiments, systematic effects are of great concern, and much care is taken to minimize and study these effects. This section outlines the procedures used to study and to reduce these effects to a level which allows a 200-part-per-billion measurement to be made.

Doppler shift

In fast atomic beam experiments the first-order Doppler shift can be very large. By aligning the microwaves very nearly perpendicular to the atomic beam this shift has been nearly eliminated. Since the axis of the beam is aligned perpendicular to $B1$ and $B2$ to within 0.3 mrad (with expected

TABLE II. Average fit centers and corrections for individual data runs. The first five columns identify the experimental configuration for the run, including the position and orientation of the Magic T, the beam speed, and the microwave power, as described in the text. The sixth column gives the average center obtained from fits of data scans to the simple cosine line shape of Eq. (4). Δ_{fit} is the uncertainty in the fit center, and Δ_{dir} is the statistical uncertainty due to possible variations of up to 0.2 mrad in the direction of the beam from run to run. The next two columns give the correction due to the ac Stark shift caused by the microwave fields and the dc Stark shift due to stray dc electric fields in the microwave interaction region. The next column gives the correction due to time dilation in the moving frame of the fast atoms. The column labeled ‘‘BB shift’’ is a correction due to ac Stark shifts induced by the presence of blackbody radiation and is calculated in the formalism of Farley and Wing [25]. The column labeled ‘‘Term. shift’’ gives the correction associated with a change of the microwave phase due to small reflections from the microwave terminators. The column entitled ‘‘Nbr. res.’’ lists small uncertainties which result from overlap with the far wings of neighboring F - G resonances. The final column gives the corrected centers for the data run. All values are given in kHz, with one standard deviation uncertainties in the last digits given in parentheses.

Data set	Magic-T position	Magic-T orientation	Beam speed	Microwave power	Fit center (Δ_{fit})(Δ_{dir})	ac shift	dc shift	Time dilation	BB shift	Term. shift	Nbr. res.	Corrected center
1	top	$E1-B1$	4.0 keV	saturation	2 017 321.68(28)(110)	0.27(3)	1.09(31)	2.17(0)	-0.17(2)	-0.30(10)	0.00(13)	2 017 324.74(120)
	top	$E1-B1$	2.3 keV	saturation	2 017 323.12(60)(110)	0.15(2)	0.95(29)	1.25(0)	-0.17(2)	-0.23(8)	0.00(4)	2 017 325.07(129)
	top	$E1-B2$	4.0 keV	saturation	2 017 324.96(43)(110)	0.27(3)	1.16(32)	2.17(0)	-0.17(2)	-0.30(10)	0.00(13)	2 017 328.09(125)
	top	$E1-B2$	2.3 keV	saturation	2 017 324.96(74)(110)	0.15(2)	1.16(32)	1.25(0)	-0.17(2)	-0.23(8)	0.00(4)	2 017 327.12(137)
	bottom	$E1-B1$	4.0 keV	saturation	2 017 323.28(53)(110)	0.27(3)	1.10(31)	2.17(0)	-0.17(2)	-0.30(10)	0.00(13)	2 017 326.35(128)
	bottom	$E1-B1$	2.3 keV	saturation	2 017 325.60(66)(110)	0.15(2)	0.85(29)	1.25(0)	-0.17(2)	-0.23(8)	0.00(4)	2 017 327.45(132)
	bottom	$E1-B2$	4.0 keV	saturation	2 017 323.26(45)(110)	0.27(3)	1.03(30)	2.17(0)	-0.17(2)	-0.30(10)	0.00(13)	2 017 326.26(125)
	bottom	$E1-B2$	2.3 keV	saturation	2 017 322.69(52)(110)	0.15(2)	1.11(31)	1.25(0)	-0.17(2)	-0.23(8)	0.00(4)	2 017 324.80(126)
2	top	$E1-B1$	4.0 keV	saturation	2 017 324.22(68)(110)	0.27(3)	1.44(35)	2.17(0)	-0.17(2)	-0.30(10)	0.00(13)	2 017 327.63(136)
	top	$E1-B1$	2.3 keV	saturation	2 017 325.81(81)(110)	0.15(2)	1.16(32)	1.25(0)	-0.17(2)	-0.23(8)	0.00(4)	2 017 327.97(141)
	top	$E1-B2$	4.0 keV	saturation	2 017 322.29(33)(110)	0.27(3)	1.16(32)	2.17(0)	-0.17(2)	-0.30(10)	0.00(13)	2 017 325.42(121)
	top	$E1-B2$	2.3 keV	saturation	2 017 321.26(75)(110)	0.15(2)	1.04(30)	1.25(0)	-0.17(2)	-0.23(8)	0.00(4)	2 017 323.30(137)
	bottom	$E1-B1$	4.0 keV	saturation	2 017 321.14(45)(110)	0.27(3)	0.98(30)	2.17(0)	-0.17(2)	-0.30(10)	0.00(13)	2 017 324.09(125)
	bottom	$E1-B1$	2.3 keV	saturation	2 017 322.38(78)(110)	0.15(2)	0.71(29)	1.25(0)	-0.17(2)	-0.23(8)	0.00(4)	2 017 324.09(138)
	bottom	$E1-B2$	4.0 keV	1/4 saturation	2 017 322.32(47)(110)	0.06(1)	1.17(32)	2.17(0)	-0.17(2)	-0.30(10)	0.00(3)	2 017 325.26(125)
	bottom	$E1-B2$	2.3 keV	1/4 saturation	2 017 325.54(77)(110)	0.03(0)	0.99(30)	1.25(0)	-0.17(2)	-0.23(8)	0.00(1)	2 017 327.41(138)
3	top	$E1-B1$	4.0 keV	1/4 saturation	2 017 321.73(55)(110)	0.06(1)	1.17(32)	2.17(0)	-0.17(2)	-0.30(10)	0.00(3)	2 017 324.66(128)
	top	$E1-B1$	2.3 keV	1/4 saturation	2 017 321.68(97)(110)	0.03(0)	0.87(29)	1.25(0)	-0.17(2)	-0.23(8)	0.00(1)	2 017 323.43(150)
	top	$E1-B2$	4.0 keV	1/4 saturation	2 017 322.26(68)(110)	0.06(1)	1.39(35)	2.17(0)	-0.17(2)	-0.30(10)	0.00(3)	2 017 325.41(135)
	top	$E1-B2$	2.3 keV	1/4 saturation	2 017 322.55(116)(110)	0.03(0)	1.07(30)	1.25(0)	-0.17(2)	-0.23(8)	0.00(1)	2 017 324.49(163)
	bottom	$E1-B1$	4.0 keV	1/4 saturation	2 017 322.11(49)(110)	0.06(1)	1.33(34)	2.17(0)	-0.17(2)	-0.30(10)	0.00(3)	2 017 325.21(126)
	bottom	$E1-B2$	4.0 keV	1/4 saturation	2 017 321.82(57)(110)	0.06(1)	1.32(34)	2.17(0)	-0.17(2)	-0.30(10)	0.00(3)	2 017 324.90(129)
	bottom	$E1-B2$	2.3 keV	1/4 saturation	2 017 322.53(56)(110)	0.03(0)	0.89(29)	1.25(0)	-0.17(2)	-0.23(8)	0.00(1)	2 017 324.29(127)

TABLE III. Average fit centers and corrections for data obtained in the various experimental configurations. The experimental configuration is specified in the first column, and the values given in each row correspond to an average of all data from Table II which are taken in the particular experimental configuration. The second through ninth columns give the fitted centers and corrections as described in Table II. The final row of the table gives the average of all of the data. All of the values in the table are given in kHz, with one standard deviation uncertainties given in parentheses.

Experimental configuration	Fit center	Δ_{dir}	ac shift	dc shift	Time dil	BB shift	Term.shift	Nbr res.	Corrected center
<i>E1</i> attached to <i>B1</i> , <i>E2</i> to <i>B2</i>	2 017 322.98(19)	0.00(33)	0.17(2)	1.06(31)	1.75(0)	-0.17(2)	-0.27(9)	0.00(7)	2 017 325.52(51)
<i>E1</i> attached to <i>B2</i> , <i>E2</i> to <i>B1</i>	2 017 323.04(19)	0.00(32)	0.13(2)	1.12(31)	1.71(0)	-0.17(2)	-0.27(9)	0.00(6)	2 017 325.56(50)
Magic-T assembly on top	2 017 323.04(20)	0.00(32)	0.16(2)	1.14(32)	1.71(0)	-0.17(2)	-0.27(9)	0.00(7)	2 017 325.61(51)
Magic-T assembly on bottom	2 017 322.97(17)	0.00(33)	0.14(2)	1.04(31)	1.75(0)	-0.17(2)	-0.27(9)	0.00(6)	2 017 325.46(50)
4.001-keV He beam	2 017 322.59(15)	0.00(32)	0.18(2)	1.19(32)	2.17(0)	-0.17(2)	-0.30(10)	0.00(9)	2 017 325.66(49)
2.309-keV He beam	2 017 323.47(23)	0.00(33)	0.11(1)	0.98(30)	1.25(0)	-0.17(2)	-0.23(8)	0.00(3)	2 017 325.41(51)
Saturation microwave power	2 017 323.33(16)	0.00(29)	0.21(2)	1.07(31)	1.71(0)	-0.17(2)	-0.27(9)	0.00(9)	2 017 325.88(47)
One-quarter microwave power	2 017 322.50(24)	0.00(37)	0.05(1)	1.13(32)	1.76(0)	-0.17(2)	-0.27(9)	0.00(2)	2 017 325.00(55)
Average values	2 017 322.89(14)	0.00(23)	0.15(2)	1.09(31)	1.73(0)	-0.17(2)	-0.27(9)	0.00(6)	2 017 325.4(4)

variations from one data run to another of 0.2 mrad), the expected first-order Doppler shift is less than 900 Hz (with 600-Hz variations from one data run to another). The variation of the Doppler shift is part of the statistical uncertainty in the columns labeled Δ_{dir} in Tables II and III. Half of the data are taken with the Magic-T assembly positioned on top of *B1* and *B2* and half with it on the bottom. In these two orientations the microwaves travel in opposite directions and hence have first-order Doppler shifts of the opposite sign. The average of centers obtained in these two orientations gives a result that is independent of the first-order Doppler shift. The difference of 0.2(6) kHz between data taken in the two orientations (see the final column of the rows labeled ‘‘Magic-T assembly on top’’ and ‘‘Magic-T assembly on bottom’’ in Table III) verifies that the beam (on average) is perpendicular to the microwaves to within 0.2 mrad.

Phase of SOF fields

Another major concern is that of the relative phase of the microwaves in the two microwave regions. The SOF signal is centered at the transition frequency if the two driving fields (i.e., the microwaves at the atomic beam in *B1* and *B2*) are exactly in phase or exactly 180° out of phase. If the relative phase is not exactly 0° or 180° the observed signal will be shifted. With relative phases of 0° + δ and 180° + δ for the two microwave fields the resonance shifts by 1.24 kHz per degree of phase δ .

In the experiment a nonzero δ can result from a difference in microwave path length in the two arms (to *E1* and to *E2* of Fig. 1) of the Magic-T assembly. One degree in δ corresponds to a 0.5-mm path-length difference. A phase δ can also result from nonidealities of the Magic T itself, from poorly aligned waveguide connections or differences in the exact shape of the waveguide in the two arms. Since the Magic-T assembly is kept in one piece, the relative phase at the outputs *E1* and *E2* remains constant throughout the experiment. Because *B1* and *B2* are identical to within 25 μm and do not move by more than 50 μm and because of the precision doweled connections between *E1*, *E2* and *B1*, *B2*, the microwave path lengths from either *E1* or *E2* to the centers of *B1* or *B2* are identical. Thus any phase difference δ due to the nonidealities of the Magic-T assembly can be

canceled by reversing the direction of the assembly (attaching *E1* to *B2* and *E2* to *B1* in Fig. 1) which has the effect of changing the sign of δ . Since half of the data are taken in each of the two orientations, the average of the data is independent of the effects of δ . From Table III, we can see that the difference between centers obtained in the two orientations is 0.0(7) kHz, indicating that the phases at *E1* and *E2* are matched to within 0.3°.

There are two additional factors which affect the relative phase of the microwaves in the two SOF regions. The first is the direction of the helium beam. If, for example, the beam passes through the center of *B1*, but passes above the center of *B2*, the atoms will be affected by a relative phase shift δ between the microwaves in *B1* and those in *B2*. This effect shifts the resonance by approximately 2 kHz for each milliradian that the atomic beam is away from the axis perpendicular to *B1* and *B2*. Since the beam is perpendicular to *B1* and *B2* to within 0.3 mrad, this effect is expected to be less than 700 Hz. Like the first-order Doppler shift, this effect is canceled when one averages centers obtained with the Magic-T assembly on the top and on the bottom of *B1* and *B2*. Since the beam direction varies by up to 0.2 mrad from day to day, there is an additional statistical uncertainty in the individual measurements listed in Table II. This uncertainty of 500 Hz is combined with the correlated uncertainty of 600 Hz due to the first-order Doppler shift and is included in the column labeled Δ_{dir} in Table II.

The final factor which affects the relative microwave phase is small reflections off of the terminators TA and TB. Since the reflected wave is not in phase with the incoming microwaves (at the position of the atomic beam) the reflected microwaves shift the phase of the combined microwave fields. By studying the terminators with the slotted line we find that the reflected microwaves from the two terminators differ in both size and phase [$|\Gamma_{\text{TA}} - \Gamma_{\text{TB}}| = -0.0050(7)$, $\theta_{\text{TA-TB}} = 61^\circ(15)$]. TB is always attached to *B1* and TA to *B2*. The phase difference (the phase in *B2* minus the phase in *B1*) which results is $-0.24(8)^\circ$. A correction for this systematic shift of $-300(100)$ Hz for the 4.001-keV beam and $-230(80)$ Hz for the 2.309-keV beam is shown in the ‘‘Term.shift’’ columns of Tables II and III.

dc Stark shifts

A third effect which leads to a significant systematic effect is the result of small dc electric fields present in (or between) $B1$ and $B2$. The measured resonance has a large Stark-shift rate of $-6.4(3)$ MHz/(V²/cm²) and thus it is necessary that the electric fields be small and well monitored.

Many precautions are taken to minimize the size of possible dc electric fields. $B1$ and $B2$, as well as the 5-cm-diam tube which connects them, are made entirely of copper so that electric fields due to contact potentials between dissimilar metals are avoided. Another source of electric fields is surface charging. Thin insulating layers may be present on the copper surfaces due to oxides or thin oil coatings from the backstreaming of vacuum pump fluid. This insulating layer may become charged when fast atoms strike it and electrons are ejected in the collision. Atoms may strike surfaces in the microwave region if they are scattered out of the beam by background gas. To discourage an oil coating, the microwave system is heated to approximately 330 K between data runs and is maintained at least 10 °C above room temperature during data acquisition.

Another source of electric fields experienced by the fast helium atoms is the result of the relativistic transformation of static magnetic fields. Only nonmagnetic materials are used in the construction of the microwave region and the Earth's half-Gauss magnetic field is reduced to less than 10 mG rms in the microwave region by a set of three very large magnet coils. These magnetic fields result in motional electric fields of less than 4 mV/cm.

The electric field present in the microwave region is measured several times during each data run by monitoring the position of the $n=20$ 3D_2 -to- 3F_3 resonance in helium, which occurs at 1999.435 MHz in zero dc field and has a very large quadratic Stark-shift rate of $-360(20)$ MHz/(V²/cm²). The Stark shift of the $n=10$ $^+F_3$ -to- $^+G_4$ resonance is determined using the formula

$$\Delta E_{\text{Stark}}^{10F-G} = \frac{k_{10F-G}}{k_{20D-F}} \Delta E_{\text{Stark}}^{20D-F}, \quad (5)$$

where k_{10F-G} and k_{20D-F} are the Stark-shift rates of the $n=10$ $^+F_3$ -to- $^+G_4$ and 20 3D_2 -to- 3F_3 intervals and $\Delta E_{\text{Stark}}^{20D-F}$ is the observed Stark shift in the $n=20$ 3D_2 -to- 3F_3 interval. The uncertainty in the Stark-shift rates of both the $n=20$ $D-F$ and the $n=10$ $F-G$ resonance is due to the uncertainty in the relative populations of the m_J states, each of which has a different dc Stark-shift rate.

To measure the $n=20$ 3D_2 -to- 3F_3 resonance the CO₂ laser is tuned to the II $R(26)$ line ($\lambda=9.086$ μm) and half of the 15-W beam is input into each of the laser-interaction regions. The first laser-interaction region is Doppler tuned to excite the 9 3P -to- 20 3D transition. The 20 3D_2 atoms created here are driven to the 20 3F_3 state in the microwave separated-oscillatory-field regions. In the second laser-interaction region, the other half on the CO₂ laser beam is Doppler tuned to the 9 3P -to- 20 3D transition. Here the remaining 20 3D atoms, not excited to the 20 3F_3 state in the microwave region, are returned to the 9 3P state. The 20 3F_3 atoms are Stark ionized and deflected into the channel electron multiplier.

In both laser-interaction regions all of the triplet- P to triplet- D transitions are excited and hence the $n=20$ 3D_2 -to- 3F_3 signal is complicated by the presence of the nearby $n=20$ 3D_1 -to- 3F_2 and 20 3D_3 -to- 3F_4 signals. The beam acceleration voltages of 2.309 and 4.001 kV are chosen to minimize the effective shift due to these two neighboring resonances. At these two voltages the oscillations of the SOF signals from the two neighboring resonances are nearly in phase with the oscillations of the SOF signal from the $n=20$ 3D_2 -to- 3F_3 resonance, and thus lead to much smaller shifts. These effects are modeled using numerical integration of the Schrödinger equation. The energies (obtained from an extrapolation of Drake's variational calculations [16] using methods similar to those given in Ref. [24]), as well as lifetimes and matrix elements (obtained using a hydrogenic approximation) of the $n=20$ P , D , F , and G states, are included. The microwave fields for these transitions are 0.006 97(3) and 0.005 35(2) V/cm, for the 4.001- and 2.309-keV beams, respectively. The signal is numerically integrated at frequencies near 1999.5 MHz with initial population in each of the 20 3D states and in all m_J states. The numerical integration indicates that the expected line center of the SOF signals in zero dc electric field are 1999.449(10) and 1999.442(10) MHz for the fast and slow beams, respectively. The measured resonance is shifted on average by about -60 kHz from these zero-dc-field positions, indicating that a rms dc electric field of about 12 mV/cm is present in the SOF region.

The stray dc electric field in the SOF region is probably not uniform. Electric fields due to surface charging, for example, may be larger near $B1$ and $B2$. Various nonuniform electric fields are included in numerical integrations of the Schrödinger equation for both the $n=20$ D -to- F and the $n=10$ F -to- G intervals, and the results indicate that Eq. (5) is correct at a level of better than 20% even for nonuniform dc fields.

The correction due to dc Stark shifts is included in Tables II and III and is approximately 1 kHz. The uncertainty in the Stark shift includes the uncertainty of the Stark-shift rates, the 10-kHz uncertainty in the zero-electric-field center of the $n=20$ 3D_2 -to- 3F_3 transition, and the 20% uncertainty due to the appropriateness of using Eq. (5) for electric fields which might be nonuniform.

Other systematic effects

The measured interval is only one of the four strongly allowed $10F$ -to- $10G$ transitions. The 10 $^+F_3$ -to- $^+G_4$ transition is chosen for this work because it is separated from the other three $F-G$ intervals by more than 20 MHz, which is large compared to the Rabi envelope widths of 8 and 6 MHz. A long scan of data covering frequencies from 2000 to 2050 MHz shows all four of the strong transitions with the expected centers and Rabi linewidths. To check that these neighboring resonances do not significantly shift the $^+F_3$ -to- $^+G_4$ resonance, the Schrödinger equation was again numerically integrated with population input to each of the other $10G$ states. The effects, as expected, are small and associated uncertainties are included in Tables II and III.

The correction due to time dilation is $+\beta^2 f/2$. This systematic effect has little uncertainty since the beam speed β is

very accurately known. (See the discussion of Ω in the line-shape section.) The corrections due to time dilation of about 2 kHz are included in Tables II and III.

The ac Stark shift (or power shift) can be calculated from

$$\Delta_{\text{ac}}^i = \sum (eE_{\mu\text{wave}z_{ik}}/2)^2 / (E_i - E_k \pm hf), \quad (6)$$

where the sum is over all states k and includes both the plus and minus signs. For the resonant term, only the plus sign is used, and this term is referred to as the Bloch-Siegert shift. The ac Stark-shift rate of the $n=10 \ ^+F_{3\text{-to-}} \ ^+G_4$ resonance is $-4.86(23)$ MHz/(V²/cm²) in a constant amplitude microwave field. The uncertainty comes from the uncertainty in the relative population of the m_J states, since each m_J has a different ac Stark-shift rate. In a SOF configuration the atoms spend only a fraction of their time in the microwave fields (i.e., in $B1$ and $B2$) and spend the bulk of their time in the field-free region between $B1$ and $B2$. An estimate [23] of the ac Stark shift for a SOF geometry is that the constant-microwave-field ac shift is reduced by a factor τ/T . Using this estimate, the ac Stark shifts are reduced by 0.0557, and are 267(27) Hz for the field of 0.031 13(13) V/cm, 60(6) Hz for 0.015 62(7) V/cm, 153(15) Hz for 0.023 62(10) V/cm, and 32(3) Hz for 0.011 84(5) V/cm. The uncertainties given are the combination of the uncertainty in the electric fields and the uncertainty in the ac Stark-shift rate of the interval.

Another estimate of the ac Stark shift is obtained from numerically integrating the Schrödinger equation for atoms at each beam speed and at each power. From fits of these numerical integrations, ac Stark shifts of 260(10), 40(10), 165(10), and 25(10) Hz are found, in excellent agreement with the simple τ/T ac shift estimates. The corrections specified in the ac-shift columns of Tables II and III are those calculated using the simple τ/T estimate.

An additional ac Stark shift is caused by blackbody radiation present in the microwave region. The temperature of the SOF microwave region is monitored using three thermocouples, one on each of $B1$ and $B2$ and one halfway between $B1$ and $B2$ on the 2-in. copper tube. The average monitored temperature is 315(5) K. The associated shift is calculated in the formalism of Farley and Wing [25] and is included in the columns labeled “BB shift” in Tables II and III.

Another concern is that the microwave power in the two SOF regions ($B1$ and $B2$) might be unequal, or that the powers in $B1$ and $B2$ might change when the microwave input is switched between the E and the H input ports of the Magic T. To check the relative size of these microwave fields, a microwave probe is inserted into $B1$ and $B2$ at the center of the beamline. The power is found to be equal to better than 10% in all cases. According to time-dependent perturbation theory, the center of the SOF pattern is independent of the relative size of these microwave fields. To confirm that this power difference leads to a negligible shift, the Schrödinger equation is integrated with a power mismatch of 10%, and the effect is found to be less than 25 Hz.

Another systematic shift results from the fact that the microwave field amplitude changes slightly as the frequency of the microwaves is tuned across the resonance. This variation is measured also by using a microwave probe inserted into $B1$ and $B2$ at the beamline center and tuning through micro-

wave frequencies near the resonance. The variation of microwave power with frequency is found to be less than 0.5% per MHz. This effect is modeled using the SOF line shape of Ref. [23], and the resulting shift is found to be less than 15 Hz.

Finally, to confirm that there is no pressure-dependent effect some data are taken at nine times greater pressure, and, as expected, indicate no pressure-dependent shift.

RESULTS AND CONCLUSIONS

The last row of Table III gives the average fit center of all the experimental data in the four configurations of the Magic-T assembly, at the two beam speeds, and at the two microwave powers, as well as the average corrections due to the various systematic effects. The final measured result of the $n=10 \ ^+F_{3\text{-to-}} \ ^+G_4$ interval in helium is 2017.3254(4) MHz. This 200-part-per-billion result is the most accurate measurement of any Rydberg fine structure. The result shows poor agreement with the previous measurement of the same interval [6] of 2017.3110(31) MHz. The reason for the difference is not known. We note that systematic effects in the present measurement are small and carefully monitored, and, due to large signal-to-noise ratios, it is possible to vary a variety of parameters (including beam speed, microwave power, and pressure) to confirm their effects. The SOF geometry has many advantages, including narrow linewidths and all but eliminating the first-order Doppler shift. The line shape of the SOF experiment is very simple and agrees extremely well with the experimental data as seen in Fig. 3.

The most precise theoretical prediction [16] of this interval is also at the 200-part-per-billion level of precision. The variational calculation of Drake predicts 2017.3254(4) MHz for this splitting, which is in good agreement with the measured result. This calculation, however, does not include certain long-range retardation (Casimir) corrections which have been computed directly using long-range QED calculations [13]. These corrections (referred to as $\langle V''_{\text{ret}} \rangle$) contribute -0.0012 MHz to the present interval. V''_{ret} shows the limitation of standard atomic physics calculations for calculating long-range QED effects and represents the onset of the long-range behavior of the Casimir interaction. Combining Drake’s calculated interval and the V''_{ret} contribution gives a predicted interval of 2017.3242(4) MHz, 1.2 kHz below the measured value. This difference is three times the experimental uncertainty and is twice the combined uncertainty of theory and experiment. This discrepancy seems to indicate that the long-range Casimir interaction contribution of -1.2 kHz is not present. The only other measurement of the long-range Casimir forces on microscopic systems is that by Sukenik *et al.* [26], who measure the force between a sodium atom and two conducting planes. Their measurement confirms the presence of the long-range Casimir interaction in that system. A second possible interpretation of our present results is that the long-range Casimir interaction is in fact present and that there are also additional interactions, indicating new long-range physics in these large atoms. One example of such additional interactions could be a spin-dependent part of the long-range Casimir interaction, which has not yet been calculated. Either interpretation indicates a

problem with the present understanding of long-range QED interactions.

The level of agreement between the present measurement and Drake's theory is consistent with the agreement (at 1 ppm) in the $n=10$ D -to- F intervals [8] and in the $n=5$ F -to- G intervals (at 5 ppm) [9]. In contrast, there is a discrepancy of 5 ppm at higher L [7]. The level of agreement with the present measurement confirms the total retardation contribution to this interval (0.1853 MHz) and the one- and two-electron Lamb-shift contributions (0.0669 MHz) to an

accuracy of better than 1%. The total relativistic contribution (10.5268 MHz) is tested to an accuracy of 40 ppm and, of course, the nonrelativistic Coulomb interaction is tested at the 200-parts-per-billion level.

ACKNOWLEDGMENT

This work is supported by the Natural Sciences and Engineering Research Council of Canada.

-
- [1] J. W. Farley, K. B. MacAdam, and W. H. Wing, *Phys. Rev. A* **20**, 1754 (1979); **25**, 1790 (1982).
- [2] W. H. Wing and W. E. Lamb, Jr., *Phys. Rev. Lett.* **28**, 265 (1972); K. B. MacAdam and W. H. Lamb, *Phys. Rev. A* **12**, 1464 (1975); **13**, 2163 (1976); **15**, 678 (1977).
- [3] D. R. Cok and S. R. Lundeen, *Phys. Rev. A* **23**, 2488 (1981).
- [4] S. L. Palfrey and S. R. Lundeen, *Phys. Rev. Lett.* **53**, 1141 (1984).
- [5] E. A. Hessels, W. G. Sturuss, S. R. Lundeen, and D. R. Cok, *Phys. Rev. A* **35**, 4489 (1987); E. A. Hessels, W. G. Sturuss, and S. R. Lundeen, *ibid.* **38**, 4574 (1988).
- [6] E. A. Hessels, F. J. Deck, P. W. Arcuni, and S. R. Lundeen, *Phys. Rev. A* **41**, 3663 (1990); **44**, 7855 (1991).
- [7] E. A. Hessels, P. W. Arcuni, F. J. Deck, and S. R. Lundeen, *Phys. Rev. Lett.* **65**, 2765 (1990); **66**, 2544 (1991); *Phys. Rev. A* **46**, 2622 (1992).
- [8] N. E. Claytor, E. A. Hessels, and S. R. Lundeen, *Phys. Rev. A* **52**, 165 (1995).
- [9] Y. Kriescher, O. Hilt, and G. v. Oppen, *Z. Phys. D* **29**, 103 (1994).
- [10] C. H. Storry, N. E. Rothery, and E. A. Hessels, *Phys. Rev. Lett.* **75**, 3249 (1995).
- [11] Richard J. Drachman, *Phys. Rev. A* **26**, 1228 (1982); **31**, 1253 (1985); **38**, 1659 (1988); **47**, 694 (1993); in *Long Range Casimir Forces: Theory and Recent Experiments in Atomic Systems*, edited by F. S. Levin and D. Micha (Plenum, New York, 1993).
- [12] C. K. Au, G. Feinberg, and J. Sucher, *Phys. Rev. Lett.* **53**, 1145 (1984); E. A. Hessels, *Phys. Rev. A* **46**, 5389 (1992); R. A. Swainson and G. W. F. Drake, *Can. J. Phys.* **70**, 187 (1992); G. W. F. Drake and R. A. Swainson, *Phys. Rev. A* **44**, 5448 (1991); G. W. F. Drake and Zong-Chao Yan, *ibid.* **46**, 2378 (1992); G. W. F. Drake, *ibid.* **45**, 70 (1992).
- [13] J. F. Babb and L. Spruch, *Phys. Rev. A* **38**, 13 (1988); C. K. Au and M. A. Mesa, *ibid.* **41**, 2848 (1990).
- [14] G. W. F. Drake, *Phys. Rev. Lett.* **59**, 1549 (1987); G. W. F. Drake and A. J. Makowski, *J. Opt. Soc. Am. B* **5**, 2207 (1988); G. W. F. Drake, *Nucl. Instrum. Methods B* **31**, 7 (1988); in *Relativistic, Quantum Electrodynamical, and Weak Interaction Effects in Atoms*, edited by W. Johnson, P. J. Mohr, and J. Sucher, AIP Conf. Proc. No. 189 (AIP, New York, 1989).
- [15] G. W. F. Drake, *J. Phys. B* **22**, L651 (1989); **23**, 1943 (1990).
- [16] G. W. F. Drake, in *Long Range Casimir Forces: Theory and Recent Experiments in Atomic Systems*, edited by F. S. Levin and D. Micha (Plenum, New York, 1993).
- [17] G. W. F. Drake, *Phys. Rev. Lett.* **65**, 2769 (1990); S. P. Goldman and G. W. F. Drake, *ibid.* **68**, 1683 (1992).
- [18] G. W. F. Drake and Zong-Chao Yan, *Phys. Rev. A* **46**, 2378 (1992).
- [19] See, for example, S. R. Lundeen and F. M. Pipkin, *Phys. Rev. Lett.* **46**, 232 (1981).
- [20] N. F. Ramsey, *Molecular Beams* (Oxford University Press, London, 1956).
- [21] N. E. Rothery, C. H. Storry, and E. A. Hessels, *Phys. Rev. A* **51**, 2919 (1995).
- [22] C. W. Fehrenbach, S. R. Lundeen, and O. L. Weaver, *Phys. Rev. A* **51**, R910 (1995).
- [23] S. R. Lundeen and F. M. Pipkin, *Metrologia* **22**, 9 (1986).
- [24] G. W. F. Drake, *Adv. At. Mol. Opt. Phys.* **32**, 93 (1993).
- [25] J. W. Farley and W. H. Wing, *Phys. Rev. A* **23**, 2397 (1981).
- [26] C. I. Sukenik, M. G. Boshier, D. Cho, V. Sandoghdar, and E. A. Hinds, *Phys. Rev. Lett.* **70**, 560 (1993).